JACS
JOURNAL OF THE AMERICAN CHEMICAL SOCIETY
Article
pubs.acs.org/JACS

A General Strategy for Decoupled Hydrogen Production from Water Splitting by Integrating Oxidative Biomass Valorization

Bo You, Xuan Liu, Nan Jiang, and Yujie Sun*

Department of Chemistry and Biochemistry, Utah State University, Logan, Utah 84322, United States

Supporting Information

ABSTRACT: Conventional water electrolyzers produce H_2 and O_2 simultaneously, such that additional gas separation steps are needed to prevent H_2/O_2 mixing. The sluggish anodic O_2 evolution reaction (OER) always results in low overall energy conversion efficiency and the product of OER, O_2, is not of significant value. In addition, the potential formation of reactive oxygen species (ROS) may lead to degradation of cell membranes and thus premature device failure. Herein we report a general concept of integrating oxidative biomass upgrading reactions with decoupled H_2 generation from water splitting. Five representative biomass substrates, ethanol, benzyl alcohol, furfural, furfuryl alcohol, and 5-hydroxymethylfurfural (HMF), were selected for oxidative upgrading catalyzed by a hierarchically porous Ni_3S_2/Ni foam bifunctional electrocatalyst (Ni_3S_2/NF). All the five organics can be oxidized to value-added liquid products at much lower overpotentials than that of OER. In particular, the electrocatalytic oxidation of HMF to the value-added 2,5-furandicarboxylic acid (FDCA) was further studied in detail. Benefiting from the more favorable thermodynamics of HMF oxidation than that of OER, the cell voltage for integrated H_2 production and HMF oxidation was significantly reduced by ~200 mV relative to pure water splitting to achieve 100 mA cm^{-2}, while the oxidation product (FDCA) at the anode was much more valuable than O_2. When utilized as electrocatalysts for both cathode and anode, Ni_3S_2/NF demonstrated outstanding durability and nearly unity Faradaic efficiencies for both H_2 and FDCA production. Overall, such an integration of oxidative biomass valorization and HER via earth-abundant electrocatalysts not only avoids the generation of explosive H_2/O_2 mixture and ROS, but also yields products of high value at both electrodes with lower voltage input, maximizing the energy conversion efficiency.

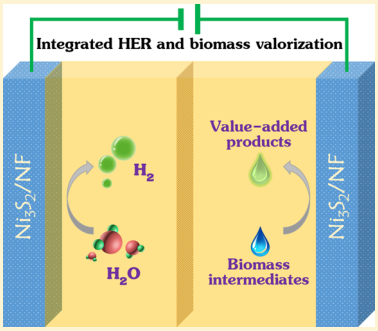

INTRODUCTION

The increasing global energy demand and critical concern of climate change resulting from fossil fuel utilization have motivated considerable efforts in developing sustainable and clean energy storage and conversion technologies.[1−4] Electrochemical or photoelectrochemical water splitting to produce clean H_2 with renewable energy input, such as solar and wind, has been considered as a promising approach for future energy needs.[5−7] By virtue of the high energy conversion efficiency, high H_2 production rate, and mature technology of proton exchange membrane (PEM) such as Nafion, room-temperature water electrolysis can be conducted under acidic conditions with PEM and catalyzed by the state-of-the-art Pt and IrO_2 (or RuO_2) catalysts for H_2 and O_2 evolution reactions (HER and OER), respectively (Figure 1a).[8−10] During water electrolysis, H_2 and O_2 are produced simultaneously, which might lead to the formation of explosive H_2/O_2 mixture (gas crossover) even when a "gas impermeable" PEM is employed.[10] Meanwhile, the coexistence of H_2, O_2, and water splitting catalysts may yield reactive oxygen species (ROS) that can degrade PEM and thus result in premature device failure, making PEM electrolyzer expensive for large-scale employment.[10] Furthermore, the overall reaction rate is often limited by the anodic OER rate because of its more sluggish kinetics.[11,12] Therefore, much higher overpotential is typically required for OER to match up the rate of HER, lowering the overall energy conversion efficiency.

Cronin et al. recently reported the utilization of electron-coupled proton buffers (ECPBs) to split conventional PEM-based water electrolysis into two separate steps using redox mediators like silicotungstic acid,[13] phosphomolybdate,[14,15] and quinone derivatives[16] (Figure 1b). Coupled with the appropriate redox processes of ECPBs, H_2 and O_2 can be generated in different time and space. For example, proton reduction occurs at a Pt cathode to produce H_2 while ECPB is oxidized to $ECPB^{n+}$ at a carbon electrode (Figure 1b, step 1), wherein no O_2 is formed. Subsequently, water oxidation takes place at another Pt anode to produce O_2 and $ECPB^{n+}$ is reduced back to the original ECPB on the same carbon electrode to complete the water electrolysis process (Figure 1b, step 2). This strategy not only prevents gas mixing in the headspace of high-pressure water electrolyzers but also allows greater flexibility regarding membranes and electrodes. Undoubtedly, the ECPB-based strategy for decoupling water splitting electrolysis is very interesting and promising for practical applications. However, the requirement of double-membranes and three-compartment configuration complicates the device construction and would

Received: July 10, 2016
Published: September 21, 2016

DOI: 10.1021/jacs.6b07127
J. Am. Chem. Soc. 2016, 138, 13639−13646

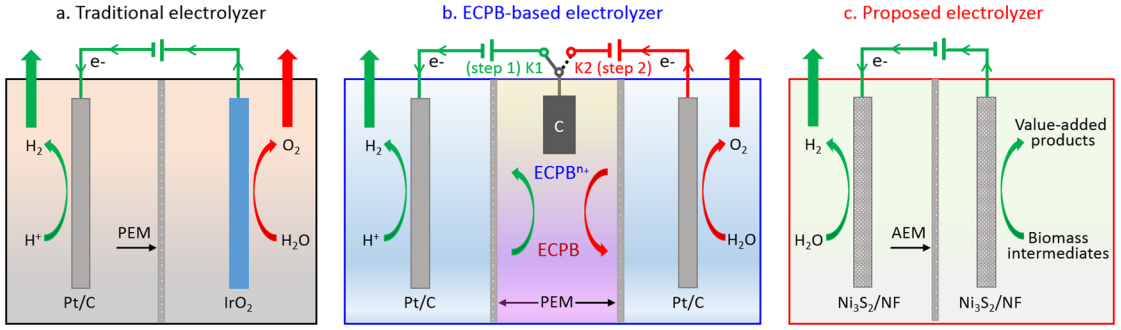

Figure 1. Illustration of (a) traditional, (b) ECPB-mediated, and (c) our proposed electrolyzers.

increase the manufacture cost. Furthermore, it still requires high overpotential to catalyze OER, whose product, O_2, is not of high value. In addition, most earth-abundant OER electrocatalysts cannot survive the strongly acidic environment of the ECPB-containing electrolytes.[17−19] Therefore, we reason that it is economically attractive to explore thermodynamically more favorable oxidation reactions which can not only replace OER but also provide electrons for HER and generate value-added nongaseous products at the anode. There are a few criteria for selecting the desirable alternative oxidation reactions: (i) the organic substrate should be soluble in aqueous media; (ii) the oxidized product should be nongaseous and more valuable than the starting compound; (iii) the oxidation potential of the organic substrate should be less positive than that of OER (otherwise the Faradaic efficiency of the new oxidation reaction will be low); and (iv) the substrate and its oxidized product will not compete with HER even though a two-compartment configuration would be preferably adopted. As schematically shown in Figure 1c, a two-compartment configuration with an anion exchange membrane (AEM) is proposed, wherein an alternative organic oxidation rather than OER occurs in the anodic compartment for the production of value-added and nongaseous products. With the appropriate selection of organic substrates and electrocatalysts, this strategy is able to reduce the voltage input for H_2 production, generate high-value products at anode, increase energy conversion efficiency, and circumvent H_2/O_2 mixing and ROS formation in traditional water electrolysis.

It is known that oxidative biomass upgrading holds a pivotal role in converting biomass-derived feedstocks to many value-added chemicals. Those oxygenated compounds can be primary building blocks to produce a diverse array of large-scale commodities, polymers, and pharmaceuticals. The traditional industrial approaches for biomass oxidation often involve stoichiometric quantities of chemical oxidants and/or utilize expensive catalysts.[20] However, due to the increasing environmental regulations and economic concerns, significant efforts have been devoted to developing "green" catalytic processes, in which catalysts are composed of earth-abundant elements and easily recyclable.[21] In order to develop inexpensive catalysts with high efficiency and excellent selectivity, chemists have been inspired by natural enzymes.[22] Million years of evolution resulted in various metalloenzymes which are capable of promoting diverse oxidation reactions with superior efficiency and exquisite selectivity under ambient conditions. The active sites of many metalloenzymes consist of earth-abundant metals, such as Mn,[23,24] Fe,[25−31] Co,[26,32,33] and Ni.[34−37] Analysis of the mechanisms of many metalloenzymes reveals that high-valent metal-oxo/hydroperoxo species often act as the key active species in many catalytic cycles.[38,39] Interestingly, high-valent metal oxo/hydroperoxo moieties have been frequently proposed critical in promoting oxidative reactions under electrocatalytic conditions.[40−49] Therefore, we reason that it is highly feasible to employ first-row transition metal-based electrocatalysts for biomass oxidation. Even more attractive is to integrate biomass oxidation with electrocatalytic H_2 production in the same electrolyzer as alluded to earlier.

As a proof of concept, we selected five biomass intermediates, ethanol, benzyl alcohol, furfural, furfuryl alcohol, and 5-hydroxymethylfurfural (HMF), as representative organic substrates[50] for electrocatalytic oxidative upgrading integrated with decoupled H_2 production from water splitting. Such a strategy avoids the issues of H_2/O_2 mixing and ROS formation and produces valuable products at both electrodes with higher energy conversion efficiency than that of sole water splitting. It should be noted that biomass is the only green and sustainable carbon source of tremendous annual production. Conversion of biomass into fuels and chemicals, generally called "biorefinery technology", has been regarded as an alternative to petroleum refining.[51−53] For instance, HMF is the dehydration product of C6 carbohydrates and can act as a platform precursor for the synthesis of a wide variety of commodity fine chemicals, plastics, pharmaceuticals, and liquid fuels.[54] For example, 2,5-furandicarboxylic acid (FDCA), one of the value-added products of HMF oxidation, can be used as an alternative monomer of terephthalic acid to produce polyamides, polyesters, and polyurethanes.[54] Even though oxidative transformation of the aforementioned five compounds have been reported, those reactions were typically conducted with stoichiometry chemical oxidants and expensive catalysts, such as Au, Pd, and Pt.[55−58] In this regard, electrocatalytic oxidation represents a more sustainable alternative as the conversion can be driven by electricity and no chemical oxidants are needed. Recently, Choi et al. reported a redox mediator-assisted electro- and photocatalytic HMF oxidation coupled with HER on Au and Pt electrodes. Nearly quantitative yield and 100% Faradaic efficiency were obtained under ambient conditions. This seminal work demonstrates the feasibility of integrating HMF oxidation with HER.[59] However, the usage of expensive metal electrodes and redox mediator (e.g., TEMPO) would result in high cost for the whole process. We reason that it is highly desirable and appealing to develop low-cost electrocatalytic systems and generalize this strategy to various organic substrates, which has received scarce attention yet.[60,61]

Herein, we report the electrocatalytic oxidation of five representative biomass compounds to value-added products catalyzed by hierarchically porous Ni_3S_2/Ni foam (Ni_3S_2/NF) under alkaline condition. Accompanying the biomass oxidation

DOI: 10.1021/jacs.6b07127
J. Am. Chem. Soc. 2016, 138, 13639−13646

at the anode, H_2 production can take place at the cathode which is also catalyzed by Ni_3S_2/NF due to its bifunctionality.[62] In this scenario (Figure 1c), H_2 and value-added organic products are produced simultaneously and no O_2 is generated at the anode. It should also be noted that our Ni_3S_2/NF electrocatalyst can be readily prepared by a one-step sulfurization of commercial nickel foam. Our strategy has at least four advantages: (1) due to the more favorable thermodynamics of these selected biomass oxidation reactions, the electrolyzer of integrated biomass oxidation and HER is able to deliver a large current density (e.g., 100 mA cm^{-2}) at a voltage ~200 mV smaller than that of pure water splitting electrolysis, hence increasing the energy conversion efficiency; (2) the oxidation products are more valuable than the starting organic substrates and significantly more useful than O_2, therefore maximizing the investment return; (3) because of the high solubility and high boiling point of those oxidation products (organic acids), they will stay in the electrolyte phase and no gas mixing or ROS issues will emerge; and (4) the alkaline electrolyte makes it possible to employ many nonprecious electrocatalysts. These advantages render our strategy very promising and practical for sustainable energy conversion technologies. We envision that this concept is potentially extendable to combine HER with many other organic oxidation reactions catalyzed by diverse inexpensive bifunctional electrocatalysts for multiple energy-related applications.

EXPERIMENTAL SECTION

Chemicals. 5-Hydroxymethylfurfural (HMF), furfuryl alcohol (FFA), potassium hydroxide (KOH), and sulfur were purchased from Alfa Aesa. 2,5-Furandicarboxylic acid (FDCA) was purchased from Chem-Impex International. 2,5-Diformylfuran (DFF) and 2-formyl-5-furancarboxylic acid (FFCA) were purchased from Ark Pharm. 5-Hydroxymethyl-2-furan-carboxylic acid (HMFCA) was purchased from Asta Tech. Ethanol (EtOH) was purchased from Decon Laboratories. Benzyl alcohol (BA) and furural (FF) were purchased from TCI. Nickel foam with purity >99.99% was purchased from MTI. All chemicals were used as received without any further purification. Deionized water (18 MΩ·cm) from a Barnstead E-Pure system was used in all experiments.

Synthesis of Ni_3S_2/NF. In a typical preparation, a piece of nickel foam (NF) with the size of 0.5 cm × 0.5 cm was placed at the center of a tube furnace and 0.5 g sulfur was placed at the upstream side of the furnace at a carefully adjusted location. After flushing with Ar for 15 min, the temperature of the furnace was quickly elevated to the reaction temperature of 280 °C with a ramping rate of 10 °C min^{-1} and kept at 280 °C for 10 min to partially convert the metallic nickel to nickel sulfides. After cooling down to room temperature, the desired Ni_3S_2/NF was obtained.

Physical Methods. Scanning electron microscopy (SEM) and elemental mapping measurements were collected on a FEI QUANTA FEG 650. X-ray diffraction (XRD) patterns were recorded on a Rigaku MiniFlexII Desktop X-ray diffractometer. X-ray photoelectron spectroscopy (XPS) was conducted using a Kratos Axis Ultra instrument. The XPS samples were affixed on a stainless steel Kratos sample bar, loaded into the instrument's load lock chamber, and evacuated to 5 × 10^{-8} Torr before transferred into the sample analysis chamber under the ultrahigh vacuum condition (~10^{-10} Torr). XPS spectra were collected using the monochromatic Al Kα source (1486.7 eV) at a 300 μm × 700 μm spot size. Low-resolution survey and high-resolution region scans at the binding energy of interest were collected for each sample. To minimize charging, all samples were flooded with low-energy electrons and ions from the instrument's built-in charge neutralizer. The samples were also sputter cleaned inside the analysis chamber with 1 keV Ar^+ ions for 30 s to remove adventitious contaminants and surface oxides. XPS data were analyzed using CasaXPS and the energy correction on high-resolution scans was calibrated by referencing the C 1s peak of adventitious carbon to 284.5 eV.

Electrocatalytic Experiments. Electrochemical HER, OER, and biomass oxidation measurements were performed on a Gamry Interface 1000E potentiostat with a three-electrode configuration. The as-prepared Ni_3S_2/NF was directly used as the working electrode, a Ag/AgCl (sat. KCl) electrode as the reference electrode, and a carbon rod as the counter electrode. All the potentials reported herein were quoted with respect to the reversible hydrogen electrode (RHE) through RHE calibration. The calibration was performed in high-purity H_2 saturated electrolyte (1.0 M KOH) with a Pt wire as the working electrode. Cyclic voltammetry (CV) was conducted at a scan rate of 1 mV s^{-1} and the average of the two potentials at which the current crossed zero was taken to be the thermodynamic potential for the hydrogen electrode reaction. The electrochemical HER, OER, and biomass oxidation experiments were conducted in 10 mL 1.0 M KOH solution with and without 10 mM organic substrates. For two-electrode electrolysis, Ni_3S_2/NF was employed as the catalyst for both anode and cathode. The linear sweep voltammetry (LSV) with the two-electrode configuration was scanned at a scan rate of 2 mV s^{-1}. *iR* (current times internal resistance) compensation was applied in all the electrochemical experiments to account for the voltage drop between the reference and working electrodes using Gamry Framework Data Acquisition Software 6.11. The stability test of Ni_3S_2/NF for biomass oxidation was evaluated by chronoamperometry at 1.423 V vs RHE in 10 mL 1.0 M KOH with 10 mM organic substrates for five successive trials.

Product Quantification. To analyze the products of HMF oxidation quantitatively and calculate the corresponding Faradaic efficiencies, 10 μL of the electrolyte solution during chronoamperometry at 1.423 V vs RHE (for three-electrode configuration) or at the cell voltage of 1.5 V (for two-electrode configuration) was withdrawn from the electrolyte solution and diluted with 490 μL water, which was then analyzed using high-performance liquid chromatography (HPLC) on a Shimadzu Prominence LC-2030C system at room temperature. The HPLC was equipped with an ultraviolet−visible detector set at 265 nm and a 4.6 mm × 150 mm Shim-pack GWS 5 μm C 18 column. A mixture of eluting solvents (A and B) was utilized. Solvent A was 5 mM ammonium formate aqueous solution and solvent B was methanol. Separation and quantification were accomplished using an isocratic elution of 70% A and 30% B for 10 min run time and the flow rate was set at 0.5 mL min^{-1}. The identification and quantification of the products were determined from the calibration curves by applying standard solutions with known concentrations of commercially purchased pure reactants, intermediates, and final products. The ^1H NMR spectra were collected on a Bruker Avance III HD Ascend 500 MHz NMR.

The conversion (%) of organic substrates and the yield (%) of oxidation products were calculated based on the following two equations:

$$\text{Conversion (\%)} = \frac{\text{mole of substrate consumed}}{\text{mole of initial substrate}} \times 100\%$$

$$\text{Yield (\%)} = \frac{\text{mole of product formed}}{\text{mole of initial substrate}} \times 100\%$$

The Faradaic efficiency (FE) of product formation was calculated using the following equation:

$$\text{FE (\%)} = \frac{\text{mole of product formed}}{\text{total charge passed}/(n \times F)} \times 100\%$$

where n is the number of electron transfer for each product formation and F is the Faraday constant (96 485 C mol^{-1}).

RESULTS AND DISCUSSION

In order to develop bifunctional electrocatalysts for both anode and cathode reactions, we chose Ni_3S_2/NF as a readily prepared

DOI: 10.1021/jacs.6b07127
J. Am. Chem. Soc. 2016, 138, 13639−13646

and low-cost model electrocatalyst. After sulfurization, the XRD pattern of the resulting foam confirmed the partial transformation of nickel foam to Ni_3S_2 (PDF no. 44−1418, Figure S1). Low-magnification SEM images of Ni_3S_2/NF indicated an interconnected, macroporous 3D framework (Figure 2a),

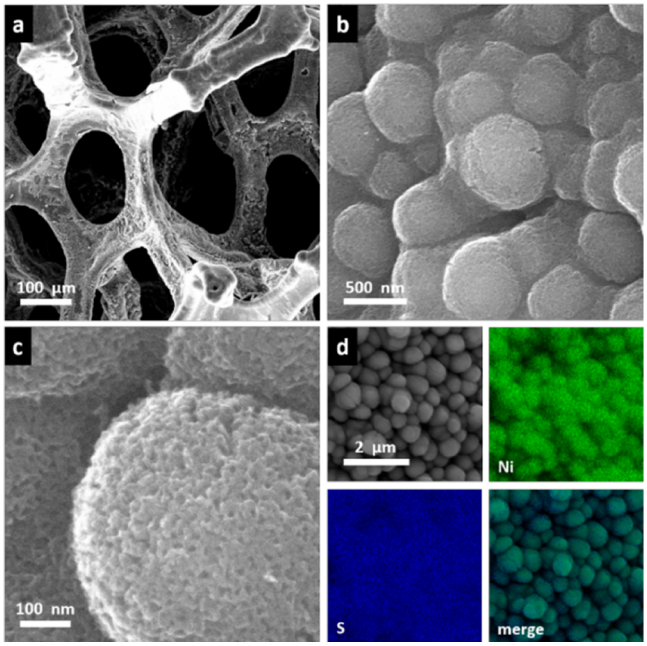

Figure 2. (a−c) SEM images of as-prepared Ni_3S_2/NF at different magnifications. (d) SEM and the element mapping images of as-prepared Ni_3S_2/NF showing the element distributions of Ni and S.

similar to that of the pristine nickel foam (Figure S2). In sharp contrast to the featureless morphology of nickel foam (Figure S2 inset), high-magnified SEM images of Ni_3S_2/NF revealed an interesting structure composed of stacked nanoparticles (Figure 2b). A closer inspection of these nanoparticles in a high-resolution SEM image exhibited the presence of numerous mesopores on the surface of Ni_3S_2/NF (Figure 2c). Such a unique hierarchically porous nanoarchitecture has been reported to facilitate the accessibility of catalytically active sites and benefit mass transport, thereby promoting the electrochemical activity.[62] Elemental mapping analysis of Ni_3S_2/NF showed the uniform distribution of Ni and S (Figure 2d), corroborating the successful chemical conversion of Ni into Ni_3S_2. In line with the elemental mapping results, XPS analysis further verified the presence of Ni and S in Ni_3S_2/NF (Figure S3). High-resolution Ni $2p_{3/2}$ spectrum was deconvoluted into three subpeaks at binding energies of 852.9, 855.8, and 861.0 eV (Figure S3a), assignable to $Ni^{\delta+}$ in Ni_3S_2, oxidized Ni species, and Ni $2p_{3/2}$ satellite peak, respectively.[62] Similarly, the high-resolution S 2p XPS spectrum (Figure S3b) could be fitted by three subpeaks at 161.9, 162.8, and 165.6 eV, corresponding to S $2p_{3/2}$, S $2p_{1/2}$, and oxidized sulfur species, respectively.[60] Collectively, all of these results supported the successful formation of Ni_3S_2/NF. It is noteworthy that the oxidized Ni and S species in Ni_3S_2/NF could be ascribed to superficial oxidation due to air contact.

We then investigated the electrocatalytic oxidation of the five representative biomass substrates, ethanol (EtOH), benzyl alcohol (BA), furfural (FF), furfuryl alcohol (FFA), and HMF, using Ni_3S_2/NF as the electrocatalyst in 1.0 M KOH. For comparison purpose, water oxidation in the absence of any organic compounds was also conducted with Ni_3S_2/NF under the same condition. Similar to our previously reported transition metal sulfides and phosphides for water oxidation, an initial electrochemical activation phenomenon was observed for Ni_3S_2/NF under anodic treatment.[62,63] Therefore, all the following LSV curves were collected after the cessation of each catalyst activation in pure 1.0 M KOH without organic substrates. As shown in Figure 3a−e, Ni_3S_2/NF exhibited an onset potential of ∼1.50 V vs RHE and high catalytic current density beyond 1.55 V vs RHE for OER, implying its excellent water oxidation activity. After introducing 10 mM biomass substrates, the onset potentials all shifted to ∼1.35 V vs RHE and rapid current density rises were observed within 1.40 V vs RHE, indicative of more favorable biomass oxidation than OER. The corresponding oxidation reactions were shown on top of the LSV curves. To achieve benchmark current densities of 50, 100, and 150 mA cm^{-2}, the overpotentials for these biomass oxidation reactions were at least 160 mV smaller than that of OER (Figure 3), strongly highlighting the better energy conversion efficiency. Remarkably, the required potential to afford 100 mA cm^{-2} for HMF oxidation was significantly reduced by 200 mV. Chronoamperometry experiments carried out at 1.423 V for the oxidation of the five organic substrates demonstrated almost complete conversion to their corresponding high-value products after passing the theoretical amount of charge, as revealed by the HPLC and ^1H NMR results (Figures 4 and S4). Nearly unity Faradaic effiencies were achieved for those biomass oxidations. It is necessary to mention that the pristine nickel foam showed much inferior performance for

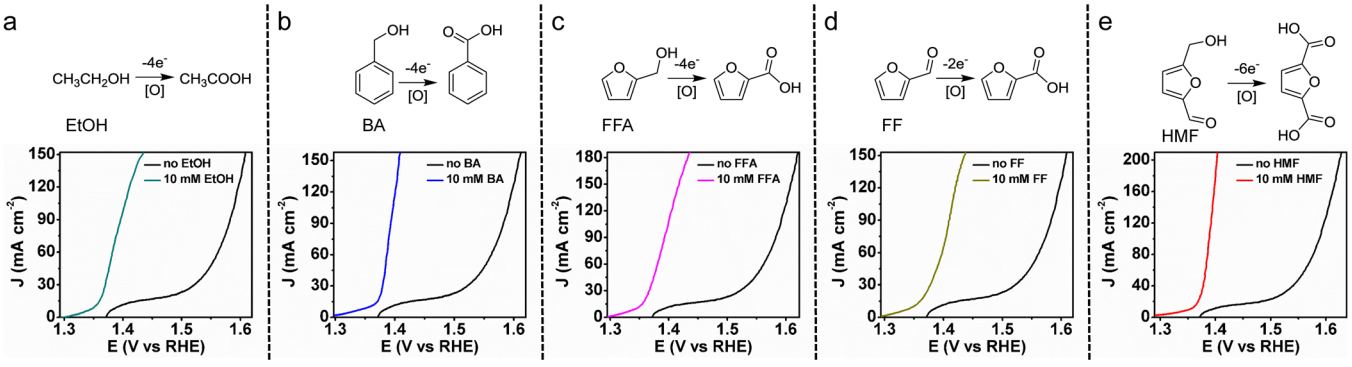

Figure 3. (a−e) Oxidation of selected organics to value-added products and the corresponding LSV curves of Ni_3S_2/NF at a scan rate of 2 mV s^{-1} in 1.0 M KOH with and without 10 mM organic substrates (BA: benzyl alcohol; FFA: furfuryl alcohol; FF: furfural; HMF: 5-hydroxymethylfurfural).

DOI: 10.1021/jacs.6b07127
J. Am. Chem. Soc. 2016, 138, 13639−13646

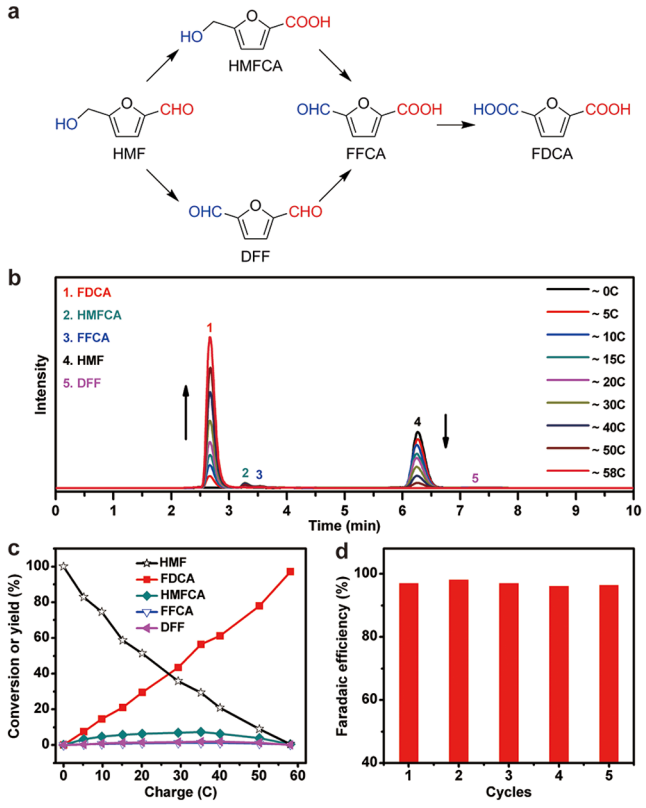

Figure 4. (a) Two possible pathways of HMF oxidation to FDCA. (b) HPLC traces of electrolysis of HMF oxidation catalyzed by Ni_3S_2/NF at 1.423 V vs RHE in 10 mL, 1.0 M KOH with 10 mM HMF. (c) Conversion and yield (%) changes of HMF and its oxidation products during the electrochemical oxidation of HMF. (d) Faradaic efficiencies of Ni_3S_2/NF for FDCA production under five successive cycles.

both OER and biomass oxidation (Figure S5), highlighting the importance of sulfurization.

In order to gain more insights into the electrocatalytic oxidation of these organic substrates, we chose HMF oxidation as a case study. Generally, aerobic oxidation of HMF follows two pathways. One is through an initial alcohol oxidation to form DFF as the intermediate (Figure 4a), while the other is from an initial aldehyde oxidation to yield HMFCA first (Figure 4a). Both pathways converge at the formation of FFCA prior to FDCA. In order to identify and quantify the oxidation intermediates and final product of HMF oxidation as well as calculate the corresponding Faradaic efficiencies, Ni_3S_2/NF-catalyzed HMF oxidation was conducted in 10 mL 1.0 M KOH with 10 mM HMF at an applied potential of 1.423 V vs RHE. ~58 C charge was calculated to convert all of the HMF to FDCA if a 100% Faradaic efficiency could be achieved. In fact, as implied in Figure 3e, no appreciable water oxidation could occur at 1.423 V, and hence a high Faradaic efficiency for HMF oxidation was anticipated. Figure 4b showed the HPLC chromatograms of HMF and its oxidation intermediates (HMFCA, DFF, and FFCA) and product (FDCA) during electrolysis. It clearly exhibited the decrease of HMF and rise of FDCA over time, suggesting the conversion of HMF to FDCA. After passing charge of ~58 C, the HPLC trace of HMF disappeared while that of FDCA rose to the maximum, which signified the complete conversion of HMF. The conversion of HMF and the yields of its oxidation intermediates as well as the final product FDCA during the electrolysis were plotted in Figure 4c, resulting in Faradaic efficiencies of 100% and 98% for HMF conversion and FDCA production, respectively.

Figure 4c also implied that the electroxidation of HMF catalyzed by Ni_3S_2/NF likely followed the first-step formation of HMFCA route (Figure 4a), as revealed by the relatively higher concentration of HMFCA compared to that of DFF during electrolysis. This pathway is in accordance with those reported aerobic HMF oxidation reactions. Nevertheless, the DFF route could not be completely excluded as we indeed observed the formation and consumption of DFF during the electrolysis.

Five successive cycles of the above constant potential electrolysis utilizing the same Ni_3S_2/NF were performed to evaluate its durability toward HMF oxidation. As shown in Figure 4d, the calculated Faradaic efficiencies for FDCA formation were in the range of 96−99%, illustrating the robust stability of Ni_3S_2/NF for HMF oxidation.

XRD, SEM, and XPS were employed to interrogate the structure and composition details of the Ni_3S_2/NF electrocatalyst after the stability testing (named as post-HMF Ni_3S_2/NF). Although the low-magnified SEM image (Figure 5a) and

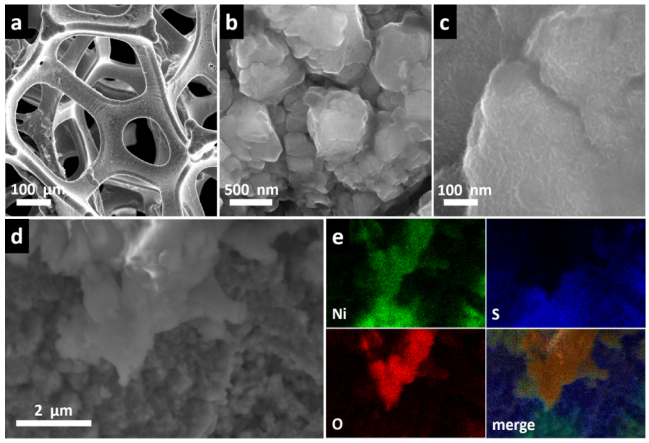

Figure 5. (a−c) SEM images of post-HMF Ni_3S_2/NF at different magnifications. (d) SEM and the element mapping images of post-HMF Ni_3S_2/NF showing the element distributions of Ni and S, plus a large amounts of O.

XRD pattern (Figure S6) of post-HMF Ni_3S_2/NF indicated the maintenance of the overall 3D hierarchically porous configuration and primary Ni_3S_2 phase, respectively, a close inspection of its high-magnified SEM images (Figure 5b−d) revealed the presence of featureless monoliths, different from the fresh sample (Figure 2c). Elemental mapping images (Figure 5e) indicated that the post-HMF Ni_3S_2/NF mainly consisted of Ni and S, plus a large concentration of O over the newly formed monoliths. On the other hand, the high-resolution Ni 2p XPS spectrum of the post-HMF Ni_3S_2/NF demonstrated the disappearance of the peak at 852.9 eV (assignable to $Ni^{\delta+}$ in Ni_3S_2) and an increase of the peak at 855.8 eV (corresponding to oxidized Ni species), suggesting the oxidation of Ni_3S_2 (Figure S7a). This oxidation phenomenon was also supported by the increased intensity of the peak ascribed to oxidized S species in the high-resolution S 2p XPS spectrum (Figure S7b). Collectively, we tentatively attribute the real catalytic active sites of Ni_3S_2/NF for HMF oxidation reaction to oxidized Ni species (nickel oxides/hydroxides and oxyhydroxides), which have also been proposed

DOI: 10.1021/jacs.6b07127
J. Am. Chem. Soc. 2016, 138, 13639−13646

as the true active species in bifunctional electrocatalysts of overall water splitting for OER.[62]

Even though a two-compartment configuration with an anion exchange membrane (AEM) employed, there still exists a certain possibility that organic species in the anode compartment would penetrate through the membrane and migrate into the cathode compartment. In order to successfully couple HER and biomass oxidation with maximum Faradaic efficiency, the electrocatalyst at the cathode should exhibit high preference for HER and strong tolerance to the presence of the selected biomass intermediates. Therefore, we sought to evaluate the impact of HMF on the HER activity of Ni_3S_2/NF under the harshest condition (assuming all the HMF was present in the cathode compartment). As demonstrated in Figure 6a, the HER

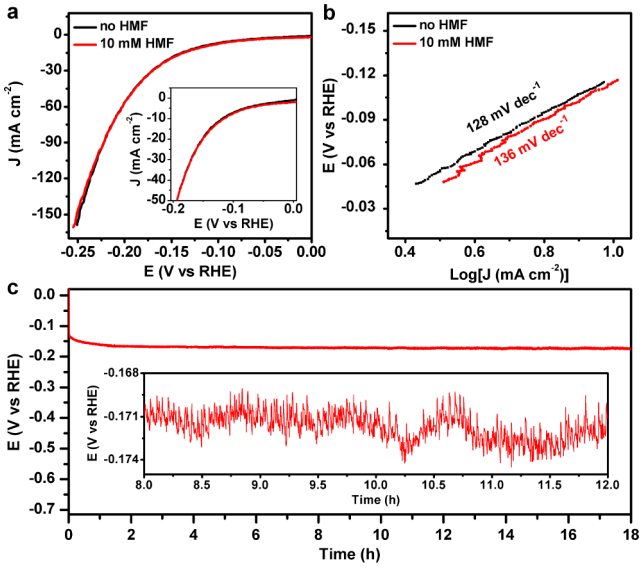

Figure 6. (a) LSV curves and (b) the corresponding Tafel plots of Ni_3S_2/NF for H_2 evolution at a scan rate of 2 mV s^{-1} in 1.0 M KOH with and without 10 mM HMF. (c) Chronopotentiometric curve of Ni_3S_2/NF for H_2 evolution at −10 mA cm^{-2} in 1.0 M KOH containing 10 mM HMF. The inset in (c) shows the expanded zigzag chronopotentiometric curve due to the growth and release of H_2 bubbles on the catalyst surface.

polarization curves of Ni_3S_2/NF in 1.0 M KOH in the absence and presence of 10 mM HMF almost overlapped and the calculated Tafel slope only increased from 128 to 136 mV dec^{-1} (Figure 6b). In addition, a 18 h chronopotentiometry experiment conducted at a current density of −10 mA cm^{-2} in 1.0 M KOH with 10 mM HMF showed that the required potential increased by less than 40 mV (Figure 6c). The fluctuation of an expanded chronopotentiometric curve also implied the formation and release of H_2 bubbles on the catalyst surface (Figure 6c inset). It should be noted that our Ni_3S_2/NF required an overpotential of only −116 mV to reach 10 mA cm^{-2}, which is lower than those of reported nonprecious HER electrocatalyts including MoC_x/C (−151 mV),[64] high-index faceted Ni_3S_2 nanosheets arrays (−223 mV),[65] and NiFe LDH/NF (−200 mV),[66] implying its excellent electrocatalytic HER activity. Similar resistance of its HER performance to the other four organic compounds was also confirmed from the analogous HER electrolysis conducted in the presence of those organic compounds (Figure S8).

Post-HER electrolysis characterization was also conducted to probe the morphology and composition details of Ni_3S_2/NF after the 18 h HER stability test in 1.0 M KOH with 10 mM HMF (denoted as post-HER with HMF Ni_3S_2/NF). The low-magnification SEM image in Figure 7a demonstrated that the

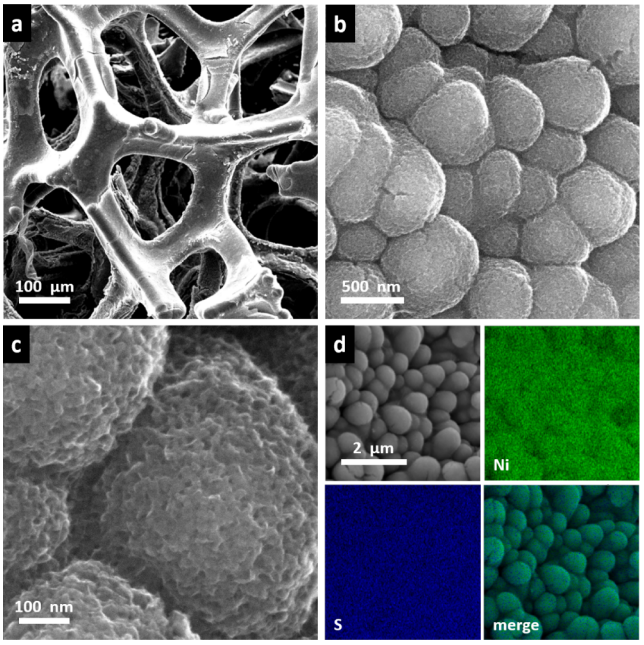

Figure 7. (a−c) SEM images of post-HER with HMF Ni_3S_2/NF at different magnifications. (d) SEM and the element mapping images of post-HER with HMF Ni_3S_2/NF showing the element distributions of Ni and S.

post-HER with HMF Ni_3S_2/NF still maintained the overall 3D hierarchically porous structure. High-magnification SEM images (Figure 7b, c) suggested that its morphology of porous nanoparticles was similar to that of the fresh Ni_3S_2/NF (Figure 2c). The corresponding elemental mapping results indicated the retained uniform spatial distribution of Ni and S in the post-HER with HMF Ni_3S_2/NF (Figure 7d). The XRD pattern demonstrated the presence of Ni_3S_2 composition, nearly identical to that of the as-prepared catalyst (Figure S6). In addition, the similarity of high-resolution Ni and S XPS spectra (Figure S7) of the fresh and post-HER with HMF Ni_3S_2/NF samples also confirmed the retention of the electrocatalysts in terms of composition and oxidation state, corroborating its superior robustness for HER electrocatalysis and excellent tolerance toward HMF.

Collectively, all the aforementioned results unambiguously demonstrated that our Ni_3S_2/NF is able to catalyze the oxidation of biomass intermediates and H_2 evolution under alkaline condition simultaneously. Hence, a two-electrode electrolyzer employing a Ni_3S_2/NF electrocatalyst couple for both anode and cathode was constructed. As shown in Figure 8a, the LSV curve of the Ni_3S_2/NF catalyst couple in 1.0 M KOH displayed an onset around 1.55 V for overall water splitting in the absence of HMF. In order to achieve catalytic current densities of 10, 20, 50, and 100 mV cm^{-2}, cell voltages of 1.58, 1.66, 1.76, and 1.84 V, respectively, were required. In fact, these voltages are smaller than those of many reported bifunctional electrocatalysts for overall water splitting, such as Co−P (1.64 V for 10 mA cm^{-2}),[63] NiFe LDH/NF (1.70 V for 10 mA cm^{-2}),[66] CoO_x@CN (1.90 V for 50 mA cm^{-2}),[67] and

DOI: 10.1021/jacs.6b07127
J. Am. Chem. Soc. 2016, 138, 13639−13646

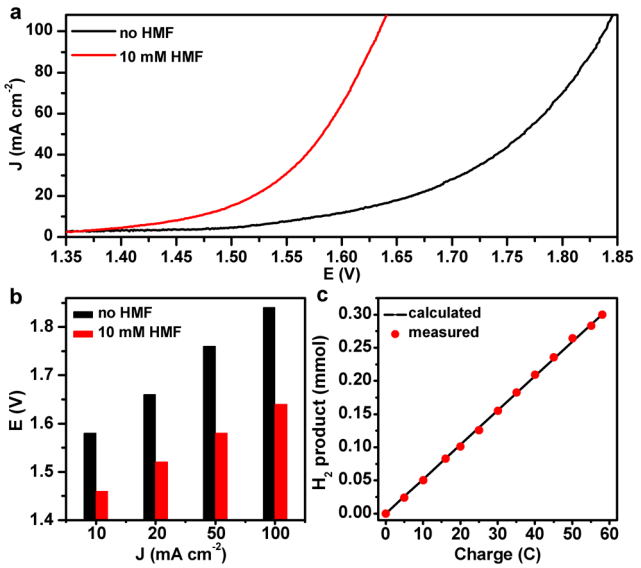

Figure 8. (a) LSV curves and (b) comparison of the overpotentials to achieve benchmark current densities for Ni_3S_2/NF couple in 1.0 M KOH with and without 10 mM HMF. (c) GC-measured H_2 quantity compared with theoretically calculated H_2 quantity assuming a 100% Faradaic efficiency for the H_2 evolution catalyzed by a Ni_3S_2/NF catalyst couple in 1.0 M KOH solution with 10 mM HMF.

Ni_5P_4/NF (1.70 V for 10 mA cm^{-2}).[68] More appealing is that upon the addition of 10 mM HMF, the catalytic onset potential was reduced to ∼1.40 V and the cell voltages were further lowered to 1.46, 1.52, 1.58, and 1.64 V to achieve 10, 20, 50, and 100 mA cm^{-2}, respectively (Figure 8b), implying much better energy conversion efficiency of Ni_3S_2/NF-catalyzed HER and HMF oxidation relative to water splitting (save 200 mV to deliver 100 mV cm^{-2}). To quantify the produced H_2 and FDCA under this two-electrode configuration, a long-term electrolysis at a constant cell voltage of 1.50 V vs RHE was executed to pass the charge of ∼58 C. As shown in Figure 8c, the generated H_2 quantified by gas chromatography (GC) matched the theoretically calculated amount very well. Analysis of the resulting electrolyte by HPLC also resulted in a ∼ 98% Faradaic efficiency for the FDCA production.

CONCLUSIONS

In summary, we have presented a general strategy for decoupled H_2 generation from water splitting by combining oxidative biomass upgrading to value-added products with a low-cost and hierarchically porous Ni_3S_2/NF bifunctional electrocatalyst. In the current case, H_2 evolution occurs at the cathode catalyzed by Ni_3S_2/NF, while simultaneously oxidative upgrading of biomass intermediates is catalyzed by the Ni_3S_2/NF-derived catalyst at the anode to more valuable bioproducts. Both reactions take place with Faradaic efficiencies close to 100%. Owing to the more favorable thermodynamics of these biomass oxidations than that of OER, the cell voltage to reach benchmark current densities (e.g., 100 mA cm^{-2}) for H_2 production is reduced by 200 mV relative to that of sole water splitting. Additionally, more valuable bioproducts (rather than O_2) are generated at the anode. Because of no O_2 production, such a new type electrolyzer could circumvent the potential H_2/O_2 mixing and ROS formation, beneficial to the long lifespan of an electrolyzer and reduce the maintenance cost. In addition, the alkaline electrolyte enables the possibility of employing nonprecious electrocatalysts. All of the above advantages render our integrating strategy very appealing to combine HER with many other organic oxidation reactions for multiple energy-related applications. It was also noted that despite the different thermodynamic changes of the oxidation reactions of those five biomass intermediates to their corresponding products, the electrocatalytic currents took off at very similar potentials (∼1.35 V vs RHE, Figure 3), which indicated that the overpotential requirement was largely determined by the oxidation of the electrocatalyst to its functional oxidation state. Therefore, it is anticipated that transition metal-based electrocatalysts that are able to reach their desired oxidation states at lower potentials would lead to smaller overpotentials for the overall reaction, which is the focus of our current investigation.

ASSOCIATED CONTENT

Supporting Information

The Supporting Information is available free of charge on the ACS Publications website at DOI: 10.1021/jacs.6b07127.

Additional figures, electrochemical plots, XRD, XPS, SEM, NMR data, HPLC chromatograms (PDF)

AUTHOR INFORMATION

Corresponding Author

*yujie.sun@usu.edu

Notes

The authors declare no competing financial interest.

ACKNOWLEDGMENTS

This work was supported by Utah State University (USU). Y.S. thanks the support of the Microscopy Core Facility at USU. N.J. acknowledges the Governor's Energy Leadership Scholars Grant of the Utah Energy Research Triangle. The NMR measurements were conducted on a NMR spectrometer supported by the NSF MRI Award CHE-1429195.

REFERENCES

(1) Lewis, N. S.; Nocera, D. G. *Proc. Natl. Acad. Sci. U. S. A.* **2006**, *103*, 15729−15735.
(2) Gray, H. B. *Nat. Chem.* **2009**, *1*, 7.
(3) Blankenship, R. E.; Tiede, D. M.; Barber, J.; Brudvig, G. W.; Fleming, G.; Ghirardi, M.; Gunner, M. R.; Junge, W.; Kramer, D. M.; Melis, A.; Moore, T. A.; Moser, C. C.; Nocera, D. G.; Nozik, A. J.; Ort, D. R.; Parson, W. W.; Prince, R. C.; Sayre, R. T. *Science* **2011**, *332*, 805−809.
(4) Chu, S.; Majumdar, A. *Nature* **2012**, *488*, 294−303.
(5) Cook, T. R.; Dogutan, D. K.; Reece, S. Y.; Surendranath, Y.; Teets, T. S.; Nocera, D. G. *Chem. Rev.* **2010**, *110*, 6474−6502.
(6) Walter, M. G.; Warren, E. L.; McKone, J. R.; Boettcher, S. W.; Mi, Q.; Santori, E. A.; Lewis, N. S. *Chem. Rev.* **2010**, *110*, 6446−6473.
(7) Thoi, V. S.; Sun, Y.; Long, J. R.; Chang, C. J. *Chem. Soc. Rev.* **2013**, *42*, 2388−2400.
(8) Barbir, F. *Sol. Energy* **2005**, *78*, 661−669.
(9) Chandesris, M.; Médeau, V.; Guillet, N.; Chelghoum, S.; Thoby, D.; Fouda-Onana, F. *Int. J. Hydrogen Energy* **2015**, *40*, 1353−1366.
(10) Berger, A.; Segalman, R. A.; Newman, J. *Energy Environ. Sci.* **2014**, *7*, 1468−1476.
(11) Kanan, M. W.; Nocera, D. G. *Science* **2008**, *321*, 1072−1075.
(12) Reece, S. Y.; Hamel, J. A.; Sung, K.; Jarvi, T. D.; Esswein, A. J.; Pijpers, J. J. H.; Nocera, D. G. *Science* **2011**, *334*, 645−648.
(13) Rausch, B.; Symes, M. D.; Chisholm, G.; Cronin, L. *Science* **2014**, *345*, 1326−1330.
(14) Symes, M. D.; Cronin, L. *Nat. Chem.* **2013**, *5*, 403−409.

DOI: 10.1021/jacs.6b07127
J. Am. Chem. Soc. 2016, 138, 13639−13646

(15) Bloor, L. G.; Solarska, R.; Bienkowski, K.; Kulesza, P. J.; Augustynski, J.; Symes, M. D.; Cronin, L. *J. Am. Chem. Soc.* **2016**, *138*, 6707−6710.
(16) Rausch, B.; Symes, M. D.; Cronin, L. *J. Am. Chem. Soc.* **2013**, *135*, 13656−13659.
(17) McCrory, C. C. L.; Jung, S.; Peters, J. C.; Jaramillo, T. F. *J. Am. Chem. Soc.* **2013**, *135*, 16977−16987.
(18) McCrory, C. C. L.; Jung, S.; Ferrer, I. M.; Chatman, S. M.; Peters, J. C.; Jaramillo, T. F. *J. Am. Chem. Soc.* **2015**, *137*, 4347−4357.
(19) Jung, S.; McCrory, C. C. L.; Ferrer, I. M.; Peters, J. C.; Jaramillo, T. F. *J. Mater. Chem. A* **2016**, *4*, 3068−3076.
(20) Punniyamurthy, T.; Velusamy, S.; Iqbal, J. *Chem. Rev.* **2005**, *105*, 2329−2364.
(21) Trindade, A. F.; Gois, P. M. P.; Afonso, C. A. M. *Chem. Rev.* **2009**, *109*, 418−514.
(22) Que, L.; Tolman, W. B. *Nature* **2008**, *455*, 333−340.
(23) Umena, Y.; Kawakami, K.; Shen, J.-R.; Kamiya, N. *Nature* **2011**, *473*, 55−60.
(24) Suga, M.; Akita, F.; Hirata, K.; Ueno, G.; Murakami, H.; Nakajima, Y.; Shimizu, T.; Yamashita, K.; Yamamoto, M.; Ago, H.; Shen, J.-R. *Nature* **2015**, *517*, 99−103.
(25) Solomon, E. I.; Brunold, T. C.; Davis, M. I.; Kemsley, J. N.; Lee, S.-K.; Lehnert, N.; Neese, F.; Skulan, A. J.; Yang, Y.-S.; Zhou, J. *Chem. Rev.* **2000**, *100*, 235−350.
(26) Kovacs, J. A. *Chem. Rev.* **2004**, *104*, 825−848.
(27) Shaik, S.; Hirao, H.; Kumar, D. *Acc. Chem. Res.* **2007**, *40*, 532−542.
(28) Solomon, E. I.; Wong, S. D.; Liu, L. V.; Decker, A.; Chow, M. S. *Curr. Opin. Chem. Biol.* **2009**, *13*, 99−113.
(29) Shaik, S.; Kumar, D.; de Visser, S. P.; Altun, A.; Thiel, W. *Chem. Rev.* **2005**, *105*, 2279−2328.
(30) Loew, G. H.; Harris, D. L. *Chem. Rev.* **2000**, *100*, 407−420.
(31) Shaik, S.; Cohen, S.; Wang, Y.; Chen, H.; Kumar, D.; Thiel, W. *Chem. Rev.* **2010**, *110*, 949−1017.
(32) Kobayashi, M.; Shimizu, S. *Eur. J. Biochem.* **1999**, *261*, 1.
(33) Riordan, C. G. In *Comprehensive Coordination Chemistry II*; Meyer, T. J., Ed.; Pergamon: Oxford, 2003; pp 677−713.
(34) Ragsdale, S. W. *J. Biol. Chem.* **2009**, *284*, 18571−18575.
(35) Maroney, M. J.; Ciurli, S. *Chem. Rev.* **2014**, *114*, 4206−4228.
(36) Shearer, J. *Acc. Chem. Res.* **2014**, *47*, 2332−2341.
(37) Wombwell, C.; Caputo, C. A.; Reisner, E. *Acc. Chem. Res.* **2015**, *48*, 2858−2865.
(38) Shaik, S.; Chen, H.; Janardanan, D. *Nat. Chem.* **2011**, *3*, 19−27.
(39) Taguchi, T.; Gupta, R.; Lassalle-Kaiser, B.; Boyce, D. W.; Yachandra, V. K.; Tolman, W. B.; Yano, J.; Hendrich, M. P.; Borovik, A. S. *J. Am. Chem. Soc.* **2012**, *134*, 1996−1999.
(40) Ellis, W. C.; McDaniel, N. D.; Bernhard, S.; Collins, T. J. *J. Am. Chem. Soc.* **2010**, *132*, 10990−10991.
(41) Fillol, J. L.; Codolà, Z.; Garcia-Bosch, I.; Gómez, L.; Pla, J. J.; Costas, M. *Nat. Chem.* **2011**, *3*, 807−813.
(42) Okamura, M.; Kondo, M.; Kuga, R.; Kurashige, Y.; Yanai, T.; Hayami, S.; Praneeth, V. K. K.; Yoshida, M.; Yoneda, K.; Kawata, S.; Masaoka, S. *Nature* **2016**, *530*, 465−468.
(43) Kanan, M. W.; Yano, J.; Surendranath, Y.; Dincă, M.; Yachandra, V. K.; Nocera, D. G. *J. Am. Chem. Soc.* **2010**, *132*, 13692−13701.
(44) Surendranath, Y.; Kanan, M. W.; Nocera, D. G. *J. Am. Chem. Soc.* **2010**, *132*, 16501−16509.
(45) Ullman, A. M.; Brodsky, C. N.; Li, N.; Zheng, S.-L.; Nocera, D. G. *J. Am. Chem. Soc.* **2016**, *138*, 4229−4236.
(46) Bediako, D. K.; Lassalle-Kaiser, B.; Surendranath, Y.; Yano, J.; Yachandra, V. K.; Nocera, D. G. *J. Am. Chem. Soc.* **2012**, *134*, 6801−6809.
(47) Bediako, D. K.; Surendranath, Y.; Nocera, D. G. *J. Am. Chem. Soc.* **2013**, *135*, 3662−3674.
(48) Huynh, M.; Shi, C.; Billinge, S. J. L.; Nocera, D. G. *J. Am. Chem. Soc.* **2015**, *137*, 14887−14904.
(49) McAlpin, J. G.; Stich, T. A.; Casey, W. H.; Britt, R. D. *Coord. Chem. Rev.* **2012**, *256*, 2445−2452.
(50) Jin, X.; Zhao, M.; Zeng, C.; Yan, W.; Song, Z.; Thapa, P. S.; Subramaniam, B.; Chaudhari, R. V. *ACS Catal.* **2016**, *6*, 4576−4583.
(51) Corma, A.; Iborra, S.; Velty, A. *Chem. Rev.* **2007**, *107*, 2411−2502.
(52) Luterbacher, J. S.; Rand, J. M.; Alonso, D. M.; Han, J.; Youngquist, J. T.; Maravelias, C. T.; Pfleger, B. F.; Dumesic, J. A. *Science* **2014**, *343*, 277−280.
(53) Xia, Q.; Chen, Z.; Shao, Y.; Gong, X.; Wang, H.; Liu, X.; Parker, S. F.; Han, X.; Yang, S.; Wang, Y. *Nat. Commun.* **2016**, *7*, 11162.
(54) van Putten, R.-J.; van der Waal, J. C.; de Jong, E.; Rasrendra, C. B.; Heeres, H. J.; de Vries, J. G. *Chem. Rev.* **2013**, *113*, 1499−1597.
(55) Hutchings, G. J. *Catal. Today* **2014**, *238*, 69−73.
(56) Villa, A.; Dimitratos, N.; Chan-Thaw, C. E.; Hammond, C.; Prati, L.; Hutchings, G. J. *Acc. Chem. Res.* **2015**, *48*, 1403−1412.
(57) Lv, G.; Wang, H.; Yang, Y.; Deng, T.; Chen, C.; Zhu, Y.; Hou, X. *ACS Catal.* **2015**, *5*, 5636−5646.
(58) Ferraz, C. P.; Garcia, M. A. S.; Teixeira-Neto, E.; Rossi, L. M. *RSC Adv.* **2016**, *6*, 25279−25285.
(59) Cha, H. G.; Choi, K.-S. *Nat. Chem.* **2015**, *7*, 328−333.
(60) You, B.; Jiang, N.; Liu, X.; Sun, Y. *Angew. Chem., Int. Ed.* **2016**, *55*, 9913−9917.
(61) Jiang, N.; You, B.; Boonstra, R.; Rodriguez, I. M. T.; Sun, Y. *ACS Energy Lett.* **2016**, *1*, 386−390.
(62) You, B.; Sun, Y. *Adv. Energy Mater.* **2016**, *6*, 1502333.
(63) Jiang, N.; You, B.; Sheng, M.; Sun, Y. *Angew. Chem., Int. Ed.* **2015**, *54*, 6251−6254.
(64) Wu, H. B.; Xia, B. Y.; Yu, L.; Yu, X. Y.; Lou, X. W. *Nat. Commun.* **2015**, *6*, 6512.
(65) Feng, L. L.; Yu, G.; Wu, Y.; Li, G. D.; Li, H.; Sun, Y.; Asefa, T.; Chen, W.; Zou, X. *J. Am. Chem. Soc.* **2015**, *137*, 14023−14026.
(66) Luo, J.; Im, J.-H.; Mayer, M. T.; Schreier, M.; Nazeeruddin, M. K.; Park, N.-G.; Tilley, S. D.; Fan, H. J.; Grätzel, M. *Science* **2014**, *345*, 1593−1596.
(67) Jin, H.; Wang, J.; Su, D.; Wei, Z.; Pang, Z.; Wang, Y. *J. Am. Chem. Soc.* **2015**, *137*, 2688−2694.
(68) Ledendecker, M.; Krick Calderón, S.; Papp, C.; Steinrück, H.-P.; Antonietti, M.; Shalom, M. *Angew. Chem., Int. Ed.* **2015**, *54*, 12361−12365.

DOI: 10.1021/jacs.6b07127
J. Am. Chem. Soc. 2016, 138, 13639−13646